RSC Publishing Faraday Discussions

Impact of Chemical Interface Damping on Surface Plasmon Dephasing

Journal:	*Faraday Discussions*
Manuscript ID	FD-ART-10-2018-000151.R1
Article Type:	Paper
Date Submitted by the Author:	24-Oct-2018
Complete List of Authors:	Therrien, Andrew; University of California Santa Barbara Kale, Matthew; University of Minnesota Yuan, Lin; Rice University, Department of Electrical and Computer Engineering Zhang, Chao; Rice University, Department of Electrical and Computer Engineering Halas, Naomi; Rice University, Department of Electrical and Computer Engineering Christopher, Phillip; University of California Santa Barbara

Impact of Chemical Interface Damping on Surface Plasmon Dephasing

Andrew J. Therrien,[a] Matthew J. Kale,[b] Lin Yuan,[e,f] Chao Zhang,[c,f] Naomi J. Halas,[c,d,e,f,g] and Phillip Christopher*[a]

[a] Department of Chemical Engineering, University of California, Santa Barbara, USA

[b] Department of Chemical Engineering and Materials Science, University of Minnesota, 421 Washington Ave. SE, Minneapolis, Minnesota 55455, United States

[c] Department of Electrical and Computer Engineering, [d] Department of Physics and Astronomy, [e] Department of Chemistry, [f] Laboratory for Nanophotonics, Smalley-Curl Institute, and [g] Department of Materials Science and NanoEngineering, Rice University, 6100 Main Street, Houston, Texas 77005, United States

Abstract

The excellent light harvesting ability of plasmonic nanoparticles makes them promising materials for a variety of technologies that rely on the conversion of photons to energetic charge carriers. In such applications, including photovoltaics and photocatalysis, the excitation of surface plasmons must induce charge transfer across the metal-adsorbate or metal-semiconductor interface. However, there is currently a lack of molecular level understanding of how the presence of a chemical interface impacts surface plasmon dephasing pathways. Here we report an approach to quantitatively measure the influence of molecular adsorption on the spectral shape and intensity of the extinction, scattering, and absorption cross-sections for nanostructured plasmonic surfaces. This is demonstrated for the case of thiophenol adsorption on lithographically patterned gold nanodisk arrays. The results show that the formation of a chemical interface between thiophenol and Au causes surface plasmons to decay more prominently through photon absorption rather than photon scattering, as compared to the bare metal. We propose that this effect is a result of the introduction of adsorbate-induced allowable electronic transitions at the interface, which facilitate surface plasmon dephasing via photon absorption. The results suggest that designed chemical interfaces with well-defined electronic structures may enable engineering of hot electron distributions, which could be important for understanding and controlling plasmon-mediated photocatalysis and, more generally, hot carrier transfer processes.

Introduction

Plasmonic materials offer a promising platform for use in a variety of technologies including photovoltaics, photocatalysis, sensing, and imaging, due primarily to the large photon extinction cross-sections and localized electromagnetic field enhancements when illuminated by a resonant photon flux.[1–5] In applications that rely on charge transfer, particularly photovoltaics and photocatalysis, localized surface plasmon excitation must lead to charge transfer at a chemical interface between the plasmonic particle and an adsorbate or semiconductor. The formation of chemical interfaces on plasmonic nanostructures is known to influence the optical properties of the material. However, there is a lack of understanding of how the surface plasmon dephasing pathways are influenced, which has important implications for photovoltaics and photocatalysis.

A surface plasmon is a coherent oscillation of electrons that only lasts for a short time, on the order of femtoseconds.[6,7] The energy distribution of charge carriers during surface plasmon excitation results in the formation of a nonthermal distribution of low-energy (<0.5 eV from E_F) excited Drude electrons.[8] After excitation, surface plasmons can dephase by either radiative scattering by re-emission of a photon, or by electron-hole pair formation induced by the absorption of the photon. In optical measurements, radiative emission is observed as photon scattering, while electron-hole pair formation is observed as photon absorption, with the sum of the two defined as the extinction. Electron-hole pair excitation occurs as a result of surface plasmon decay through surface scattering, often referred to as Landau damping, and generates hot carriers with a difference in electron and hole energy equal to the photon energy. Since the Drude electrons responsible for the plasmon oscillation represent a bulk effect and the high-energy charge carriers formed by Landau damping represent a surface scattering effect, the carrier distribution is particle size dependent.[9] The non-thermalized hot carrier distribution produced during Landau damping quickly transfers energy to low energy carriers through electron-electron scattering, resulting in thermalization on the sub-picosecond time scale. After thermalization, charge carriers couple to phonon modes of the metal and ultimately lead to heat dissipation to the surrounding environment, which occurs on the order of tens to hundreds of picoseconds.[1,10,11] For bare plasmonic nanoparticles, the dominate dephasing pathway is dictated by the size of the nanoparticle, with relatively larger particles exhibiting predominately scattering and smaller particles favoring absorption, although the exact nanoparticle size dependence of dephasing pathways is also material dependent.[12]

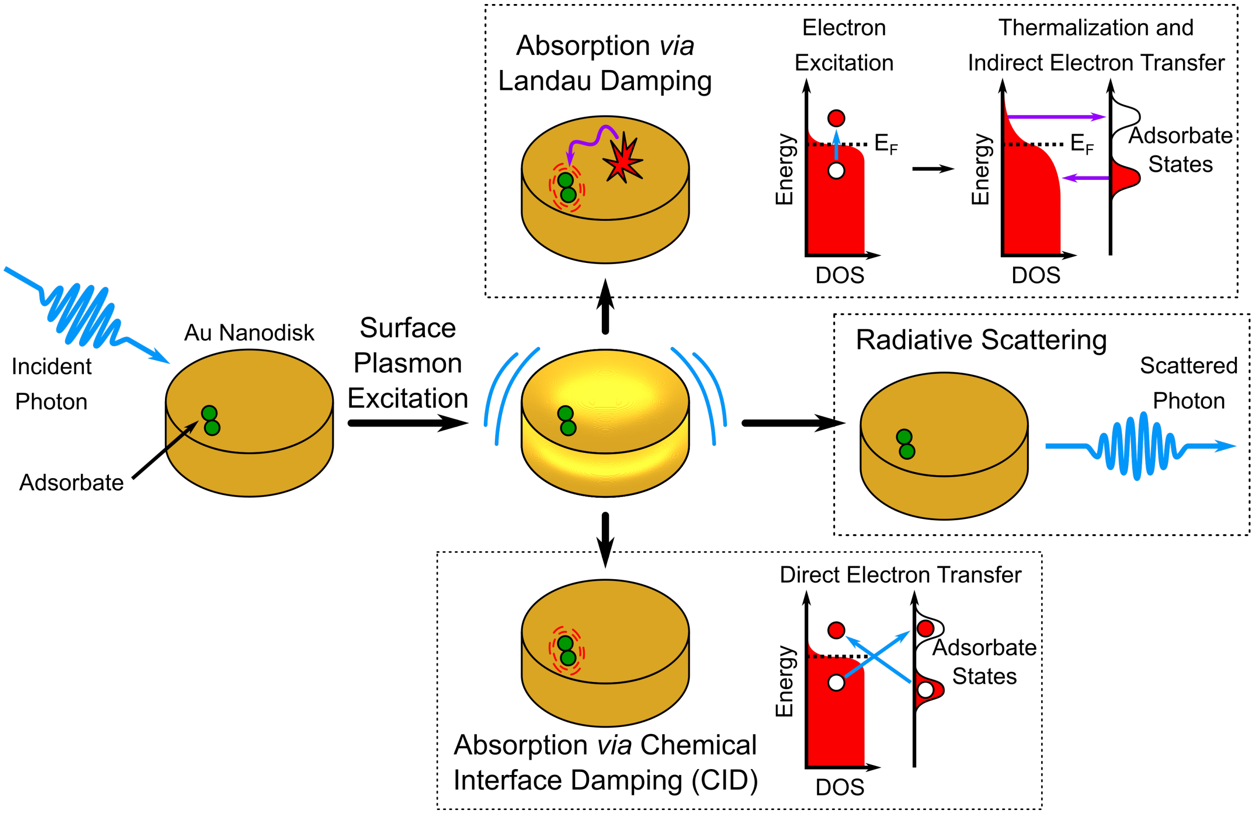

Figure 1. Schematic representation of surface plasmon excitation and three possible dephasing pathways in the presence of a surface bound adsorbate. Absorption pathways are shown with corresponding band diagrams depicting the involved electronic transitions, where E_F denotes the Fermi energy and DOS is the density of states.

In conjunction with photon scattering and photon absorption, the addition of a chemical interface to the metal, in the form of adsorbates or semiconductor, adds a new pathway for surface plasmon dephasing, called chemical interface damping (CID). The three possible surface plasmon dephasing pathways, and their implications to photocatalysis, are shown schematically in Figure 1. For simplicity, the schematic representation shows an idealized homogeneous density of states with respect to energy for the photon absorption pathways. The initial electron distributions are depicted as having some density of low energy electrons and holes surrounding the Fermi energy to represent the Drude electrons present from the surface plasmon oscillation.[8] In the case of CID, the surface plasmon dephases via photon absorption through carrier excitation directly to, or from, electronic states of the adsorbate.[13–17] After promotion of an electron to an acceptor state of the adsorbate, or removal of an electron from an adsorbate donor state, reactions can occur by transient ion processes that enable bond-selective surface chemistry.[18]

It has been proposed that charge transfer required for photocatalysis can be optimized by using small nanoparticles, due to the high density of hot charge carriers that result from the primary light extinction pathway of photon absorption.[11,19] This strategy may be particularly suitable for processes that require charge transfer at adsorbate states near the Fermi energy, as there is a relatively long-lived high concentration of electron density just above the Fermi energy during electron thermalization.[20] However, indirect charge transfer to adsorbate states has been shown to be relatively slow,[21] and therefore a significant amount of charge transfer from hot charge carriers in the metal to adsorbate states following Landau damping is unlikely.[11] On the other hand, direct charge transfer via CID has been implicated to play a predominate role in photocatalysis by wavelength dependent studies.[22] In fact, multi-photon photoemission measurements find that charge transfer occurs extremely quickly (<10 fs) when a chemical interface is present, which is too fast to be attributed to indirect electron transfer.[14,23–26] Although maximizing hot carrier production has been hypothesized to be important for photocatalysis, the potential importance of CID has not been directly established.

The optical properties of plasmonic materials are inherently tied to the surface plasmon dephasing pathways described above. With respect to a bare metal nanoparticle, experimental signatures of CID include a decrease in the extinction coefficient, a red-shift in the surface plasmon resonance energy, and spectral broadening.[27–36] The red-shift in the surface plasmon resonance energy has been attributed to multiple factors, including an increase in the local dielectric constant surrounding the nanoparticle, a decrease in the electron density in the metal due charge transfer to adsorbates, and a resonance shift due to increased damping.[32–39] The linewidth is a function of the surface plasmon coherence time,[7] for which there are four factors to consider: bulk damping, radiation damping, electron-surface scattering, and CID.[40] Bulk damping is due to electron scattering within the metal and is well described by the material's complex dielectric function; therefore it is material and frequency dependent. Radiation damping is due to coupling of the plasmon oscillation to the radiation field, which increases as a function of particle volume.[41] Electron-surface scattering leads to damping due to the larger mean free path of electrons than the dimensions of the nanoparticle, and therefore the damping is inversely proportional to the effective path length of electrons to the surface.[42] It has recently been shown that surface plasmon linewidth broadening due to CID also depends on the effective path length of electrons in the bulk of the nanoparticle to reach the surface.[34,36] This observed correlation offers insight into the nature of CID, however, such careful measurements of the homogenous surface plasmon linewidth employed single particle spectroscopy,[40] which has only been executed in scattering mode for the analysis of CID.[32,34,36] Thus, there is essentially no understanding of how CID affects the relative absorption and scattering cross-sections with respect to bare plasmonic nanoparticles.

Despite many promising and successful demonstrations of plasmonic photovoltaics and photocatalysts, it is not clear what characteristic of the plasmonic materials, beyond large extinction cross-sections, is responsible for controlling the efficiency of photocatalytic processes. The primary candidates are the degree of electromagnetic field enhancement, energy of hot charge carriers, concentration of hot charge carriers relating to the photon absorption efficiency, and CID. Determination of the critical design parameters for optimization of plasmonic materials for such applications will require a detailed understanding of each of the mentioned properties. In this study we develop insights into CID using a newly designed approach to measure the optical properties of nanostructured plasmonic surfaces. This approach allows quantitative measurements of the photon absorption and scattering cross-sections of plasmonic surfaces using a reflective sample housed in an ultra-high vacuum (UHV) chamber coupled to an integrating sphere UV-vis-NIR spectrophotometer. This approach is demonstrated through the controlled deposition of thiophenol onto well-defined Au nanodisk arrays, allowing for quantification of the influence CID has on the absorption and scattering plasmon dephasing pathways. This approach has the potential to provide deeper insights into the dominant surface plasmon dephasing pathways that contribute to plasmon-mediated photocatalysis and other charge transfer processes.

Methods

Sample Fabrication

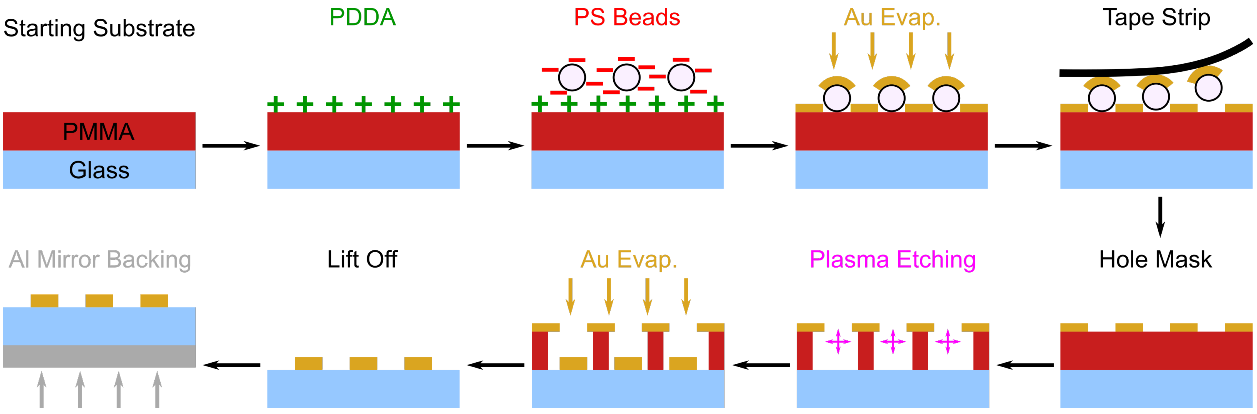

Figure 2. Schematic of hole-mask lithography for sample fabrication

The Au nanodisk array used here as a model plasmonic surface was fabricated on microscope cover glass (Fisherbrand) by utilizing a hole-mask colloidal lithography process.[43] A schematic of the approach is shown as the Figure 2. First, a layer of Poly(methyl methacrylate) (PMMA, MircoChem, 950 PMMA A4) was spin-coated on a glass substrate (2000 rpm for 1 min), then baked on a hot plate at 180° C for 10 min. The sample was then cleaned under Ar-O_2 plasma for 8 seconds (model 1020 plasma cleaner, Fischione Instruments) to make the surface of PMMA more hydrophilic. An aqueous solution of 0.2 wt% poly(diallyldimethylammonium chloride) (PDDA) was drop-casted onto the PMMA and soaked for 5 min. Deionized water was then used to rinse the surface, which was subsequently dried by N_2 gas flow. The addition of PDDA serves to functionalize the PMMA surface with a positive charge. An aqueous solution of 0.02 wt% 100 nm polystyrene (PS) beads (Sulfate Latex Beads, 8% w/v, 0.1 µm, ThermoFisher Scientific) was drop-casted onto the sample and left to sit for 10 min. Then the solution was directly removed using dry N_2 gas flow. The interplay of Coulombic attraction between the PS beads and the substrate and the Coulombic repulsion between PS beads keeps the PS dispersed across the entire PMMA surface. Next, a 20 nm Au layer was deposited followed by tape peeling to remove the PS beads from the surface, forming the hole-mask. Ar-O_2 plasma etching was employed again here for 13.5 minutes to etch the PMMA layer and expose the coverslip substrate. 50 nm of the Au was then directly deposited onto the substrate. Lift off of the PMMA and the hole-mask was achieved by soaking in acetone solution to remove the PMMA and hole-mask on top, followed by rinsing with isopropanol and N_2 gas flow to clean the surface. After Au nanodisk fabrication, in-line pass-through UV-vis-NIR measurements were performed to measure the extinction. Finally, a mirrored backing of 200 nm of Al was deposited onto the substrate.

Optical Measurements

Optical measurements were performed on reflective samples prepared by the nanofabrication procedure described above and were housed in an ultra-high vacuum (UHV) chamber with a base pressure $< 1 \times 10^{-8}$ torr. Prior to introduction into the UHV chamber, samples were rinsed with ethanol and cleaned by O_2 plasma followed by H_2 flame annealing to remove any contamination. An integrating sphere with a 3 inch light tube (Labsphere) was employed for light collection, which was pressed flush against a quartz window re-entrant into the UHV chamber, as diagrammed in Figure 3A. A Xe light source (Avantes, AvaLight-XE) and CCD detector (Avantes, AvaSpec-ULS-RS-TEC) was used for UV-vis-NIR measurements. Recorded spectra were averaged 25 times using a 14 s integration time taken over 1300 light source pulses. Experimental spectra are reported in units of 1−T, where T is the optical transmission, and spectra were collected with a bare microscope cover glass backed by 200 nm of Al as a reference. Spectra were smoothed using a Savitzky-Golay filter, fitting 2nd order polynomials over ∼18 nm windows. Spectra were converted to units of optical cross-section by dividing 1−T by the Au nanodisks density of 6.2 ± 0.2 μm^{-2}. The inherent noise in the spectra before smoothing is on the order of ∼200 nm^2 (in units of optical cross-section) and the spectrum step size is ∼0.6 nm. High precision leak valves allowed for controlled exposure to thiophenol (analytical standard, Sigma-Aldrich), which was purified by freeze-pump-thaw cycles prior to deposition. The purity of thiophenol exposure in UHV was confirmed with a quadrupole mass spectrometer (Hiden). Reported values of optical cross-section, peak position, and linewidth are the average of three separate measurements with the error bars representing the standard deviation.

FDTD Simulations

The optical properties of the Au nanodisk were simulated by using the finite-difference-time-domain (FDTD) method for solving Maxwell's equations. This study employed the package from Lumerical FDTD Solutions (Version 8.19). The Au nanodisk was modeled as a circle 100 nm in diameter and 50 nm, the "Au (Gold) – CRC" refractive index was used from the material database provided by Lumerical. Total-field/scattered-field light source conditions were used in all simulations. The incident light was injected toward +z direction, and polarized along x-axis. A uniform mesh was used with a mesh step of dx = dy = dz = 0.5 nm. The absorption and scattering were calculated within the total-field/scattered-field formalism.

Scanning Electron Microscopy (SEM)

Scanning electron microscopy (SEM) was performed using a FEI Sirion Field Emission SEM. Samples were sputter coated with PdAu prior to imaging to ensure conductivity. Imaging conditions of 5 kV electron beam at a working distance of 5 mm were used.

Results and Discussion

UV-vis-NIR Measurements

We developed an approach to measure the photon absorption and scattering cross-sections of nanostructured surfaces using a reflective sample housed in an UHV chamber. As shown in Figure 3A, an integrating sphere was used for light collection with a light tube that was re-entrant into the UHV chamber. Because the mirrored sample is positioned outside of the integrating sphere (in the UHV chamber interfaced by the light tube) only a fraction of the diffusely scattered light by the nanostructured surface is collected in the UV-vis-NIR measurement, while the remainder, x, is scattered into the UHV chamber. Since the light source is not polarized and, in the case of the Au nanodisk array examined here, the Au particle density of the sample is spatially homogenous, the light is scattered isotropically. Movement of the sample by a manipulator within the UVH chamber to different distances from the light tube inlet to the integrating sphere causes a different fraction of scattered light to be collected by the UV-vis-NIR measurements. However, the absorption contribution to all spectra is the same at all positions, as the specularly reflected light off the mirrored backing is completely collected and subject to intensity loss by photon absorption. By manipulating the distance of the sample from the inlet of the light tube, the amount of light diffusely scattered by the sample and collected by the integrating sphere varies and thus can be separated from the absorbed light. The process of light interacting with the sample in the UHV chamber is schematically shown in Figure 3B. Also noted is that in this design light is extinct twice, as it passes through the Au nanodisk array twice, which is accounted for in the data analysis.

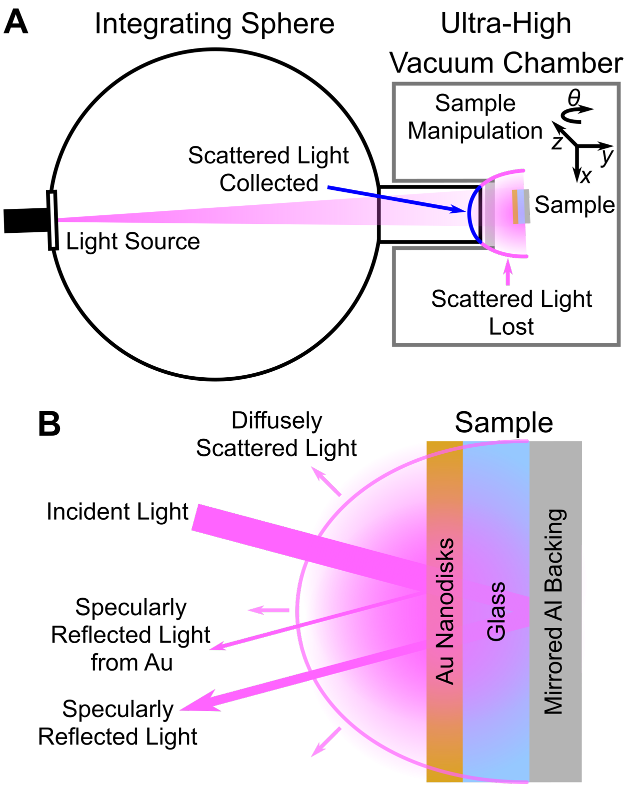

Figure 3. A) Schematic of UV-vis-NIR measurements using an integrating sphere and reflective sample. B) Diagram of light interaction with the sample.

Optical Properties of Bare Au Nanodisks

SEM imaging of the Au nanodisk array was carried out to evaluate the sample homogeneity and particle density for quantification of extinction, scattering, and absorption cross-sections. A representative SEM image is given in Figure 4A, which shows that the Au nanodisks were deposited with a density of 6.2 ± 0.2 μm^{-2}. The diameter of the Au nanodisks was also measured, and a histogram of the particle size is shown in Figure 4B. The particle size histogram matches well with the 100 nm targeted diameter, and the population was fit to Gaussian distribution with a diameter size distribution of 102 ± 16 nm.

Using the described methodology for UV-vis-NIR measurements, a reference for the absorption and scattering contributions to extinction is required. FDTD simulations were performed and used as a reference for the experimental measurements, shown in Figure 4C. The simulations were used only to calibrate the relative fraction of scattered light that was collected by the integrating sphere as a function of sample position. The use of FDTD simulations as a reference is validated by previous studies that show theory agrees well with experimentally measured scattering and absorption cross-sections of plasmonic nanostructures.[12] Transmission UV-vis-NIR measurements made before the addition of the mirrored backing of 200 nm of Al were performed to calibrate the total light extinction, shown in Figure 4D.

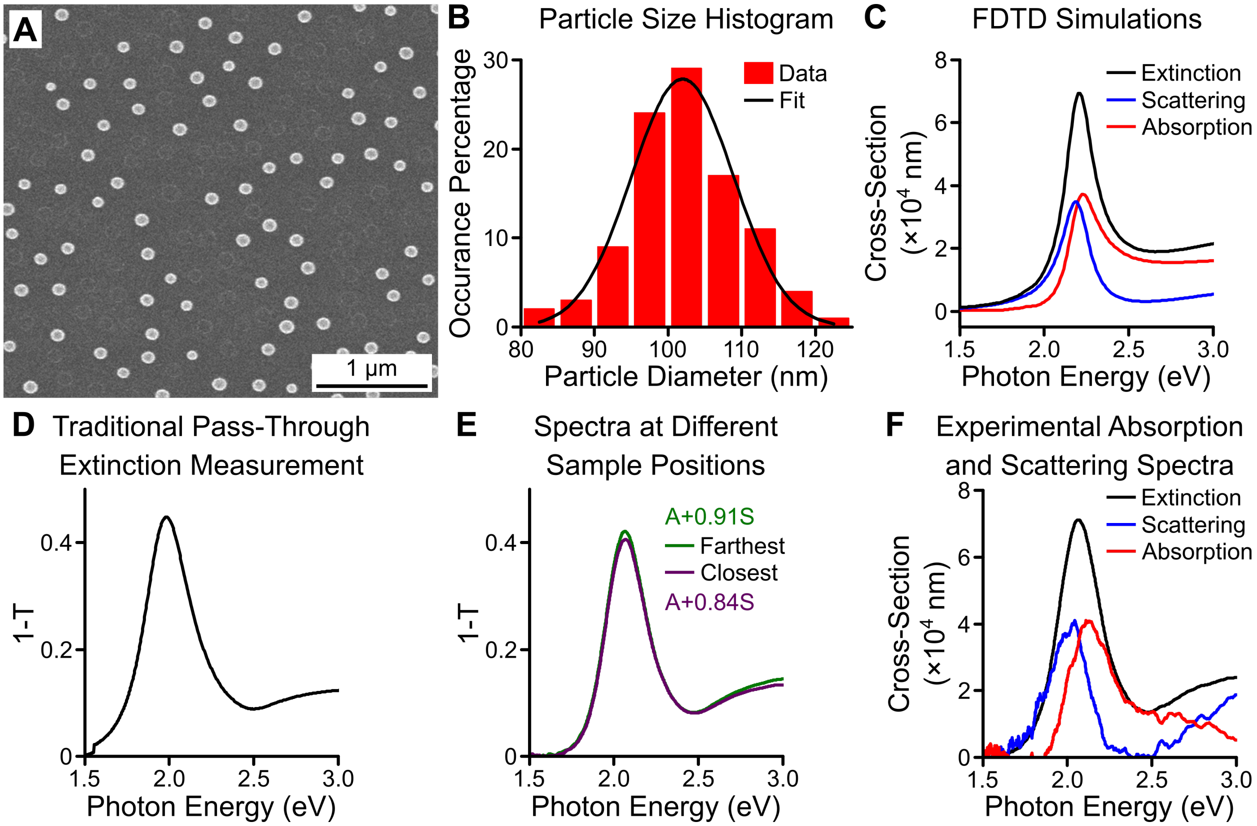

Figure 4. A) A representative SEM image of a 100 nm diameter Au nanodisk sample. B) Histogram of Au nanodisk size measured by SEM. C) FDTD simulation for a 100 nm diameter by 50 nm thick Au disk. D) Traditional pass-through UV-vis-NIR measurement of sample extinction. E) Integrating sphere measurements at different sample positions. F) Experimental deconvolution of scattering and absorption from total extinction.

As previously discussed, the amount of diffusely scattered light by the Au nanodisc array collected in the measurement is a function of the sample distance from the integrating sphere inlet. The absorption and scattering contributions to UV-vis-NIR extinction spectrum at a given sample position can be written as $A + xS$, where A is the absorption, S is the total scattering, and x is the fraction of diffusely scattered light not collected by the integrating sphere. The largest amount of diffusely scattered light loss (x is greatest) occurs when the sample position is farthest from the integrating sphere inlet, making it the most similar to an extinction measurement. When the sample is closer to the integrating sphere, more diffusely scattered light is collected (x is smaller). Thus, the difference in the spectra at different sample positions is proportional to photon scattering by the nanostructures. The spectra closest to and farthest from the integrating sphere for the Au nanodisk array are shown in Figure 4E, along with the scattering and absorption contributions. The amount of diffusely scattered light by the sample that was not collected in the measurement, x, at a given sample position was determined in the following way. The scattering spectrum for a given sample was assumed to be the difference in the measured spectra at two different sample positions divided by the change in scattered light collected by the detector, Δx. The absorption spectrum was then calculated as the measured spectrum at a given position minus x at that position multiplied by the scattering spectrum. This definition yielded an absorption to scattering ratio that was used with x as a fitting parameter to match the absorption to scattering ratio predicted from FDTD simulations.

In our experimental system the difference in the amount of diffusely scattered light collected in the measurement at the closest and further positions from the light tube, Δ*x*, was determined to be 0.07 (or 7%). Therefore, the scattering spectrum from the Au nanodisc array was calculated by taking the difference between the closest and farthest spectra and dividing by Δ*x*. To produce the absorbance spectrum, the scattering spectrum was multiplied by *x* at a given sample position and then subtracted from either of the raw UV-vis-NIR spectra shown in Figure 4E, both giving identical results. Then the sum of the scattering and absorption spectra yielded extinction. This extinction spectrum was calibrated to the transmission extinction measurement (Figure 4D) to enable calculation of optical cross-sections. Spectra were converted to units of cross-section by dividing 1−T by the Au nanodisks density of 6.2 ± 0.2 μm^{-2}. From these measurements the total extinction, absorption, and scattering of the Au nanodisks were determined and are shown in Figure 4F. The extinction cross-section was measured to be 7.3×10^4 nm^2 at the peak maximum of 1.98 eV. The geometric cross-section for 102 nm Au disks is 8.2×10^3 nm^2, which yields an extinction efficiency of 8.9, defined as the ratio of optical to geometric cross-sections. Note that the total extinction is red-shifted from FDTD simulations (Figure 4C) by 0.09 eV due to the refractive index of the glass support.

The shape and relative positions of the scattering and absorption spectra match well with the FDTD simulation (Figure 4C), which validates the experimental approach. We performed analogous measurements with Ag nanodisks, which showed similar agreement between the experimental and simulated scattering and absorption spectra in both relative position and peak shape. By this analysis, the scattering and absorption cross-sections of the Au nanodiscs were determined to be 3.9×10^4 nm^2 and 4.0×10^4 nm^2 at their peak maximums, respectively. The results are in excellent agreement with previous measurements of similarly sized Au nanodisks,[12] and also in very good agreement with the FDTD simulation (Figure 4C), which predicts scattering and absorption cross-sections of 3.5×10^4 nm^2 and 3.7×10^4 nm^2, respectively. The measured optical cross-sections correspond to a scattering efficiency of 4.5 and absorption efficiency of 4.8 for the bare Au nanodisks.

Chemical Interface Damping Induced by Thiophenol Adsorption

Thiophenol was adsorbed onto the plasmonic Au nanodisks to study the influence of CID on the extinction, absorption and scattering cross-sections of the Au nanodisks. Single-crystal studies have shown that thiophenol adsorbs dissociatively to Au(111), breaking the S-H bond.[44–46] Thiophenol readily forms ordered structures on Au, with the phenyl ring of the absorbed thiolate tilted off the surface normal.[44–46] To saturate the Au nanodisks with thiophenol, the sample was exposed to increasing amounts of gas-phase thiophenol in the UHV chamber until no further spectral changes were observed, as shown in Figure 5A. This was achieved after total exposure to thiophenol of approximately 300 Langmuirs (1 Langmuir = 1×10^{-6} torr s). After addition of thiophenol, UV-vis-NIR measurements were made to determine the extinction, scattering, and absorption cross-sections, shown in Figure 5B and C for the bare Au nanodisks and after adsorption of a saturated layer of thiophenol, respectively. By comparing the optical cross-sections of the bare and thiol covered Au nanodisks it is visually clear that the ratio of absorption to scattering cross-section increased after thiophenol adsorption. The scattering and absorption cross-sections of the thiophenol saturated Au nanodisks were determined to be 3.4×10^4 nm^2 and 4.1×10^4 nm^2 at their peak maximum, respectively.

The benefit of our approach is that the effects of CID on both scattering and absorption cross-sections can be quantitatively measured and compared. The changes in optical cross-section, surface plasmon resonance energy, and FWHM were quantified and are shown in Figure 5D. Reported values are the average of three separate measurements with the error bars representing the standard deviation. The total light extinction and scattering spectra show a decreased cross-section, surface plasmon energy red-shift, and increase in the FWHM after thiophenol adsorption, as characteristic of CID. However, the absorption spectra remained relatively unchanged after thiophenol adsorption within error. Thiophenol adsorption had a relatively small impact on the surface plasmon peak broadening, resulting in an increase of ~0.01 eV for the total extinction spectrum. The surface plasmon linewidth of Au is known to increase with increasing plasmon resonance energy due to bulk damping and the onset of interband transitions.[41,47] However, the bulk damping induced surface plasmon frequency red-shift is small, <0.01 eV, and therefore any influence on the FWHM due to bulk damping is negligible. The broadening observed here is consistent with previous measurements that correlated the influence of alkanethiol adsorption on the scattering spectra of various sizes of Au nanorods and the effective path length of electrons to the particle surface.[34] For our Au nanodisks the effective path length of electrons to the surface is about 50 nm, which would predict a surface plasmon linewidth broadening from alkanethiol adsorption of about 0.01 eV, consistent with our results.[34]

It is clear from the measurements reported here that the photon scattering dephasing pathway of surface plasmons is more significantly influenced by thiophenol adsorption than the photon absorption dephasing pathway. This can be interpreted as thiol adsorption inducing an increase in the ratio of surface plasmon dephasing by absorption compared to scattering, as shown in Figure 5D. The bare Au nanodisks had an absorption to scattering cross-section ratio of 1.03, but after the addition of a chemical interface via thiophenol adsorption that ratio increases to 1.20. While this may seem like a small effect, this is induced by a very small amount of thiophenol with respect to the amount of Au in the nanodisks. Assuming a thiophenol packing of 0.71 nmol cm^{-2} on Au,[44] the thiophenol to Au ratio in the nanodiscs is $\sim 2 \times 10^{-8}$, showing that modification of only a small fraction of Au within the nanoparticle can significantly influence the surface plasmon dephasing process. The very small amount of thiophenol with respect to Au indicates that the enhancement in the relative photon absorption is localized at the chemical interface. Based on previous work it would be expected that using smaller particles would magnify the effect further.[34]

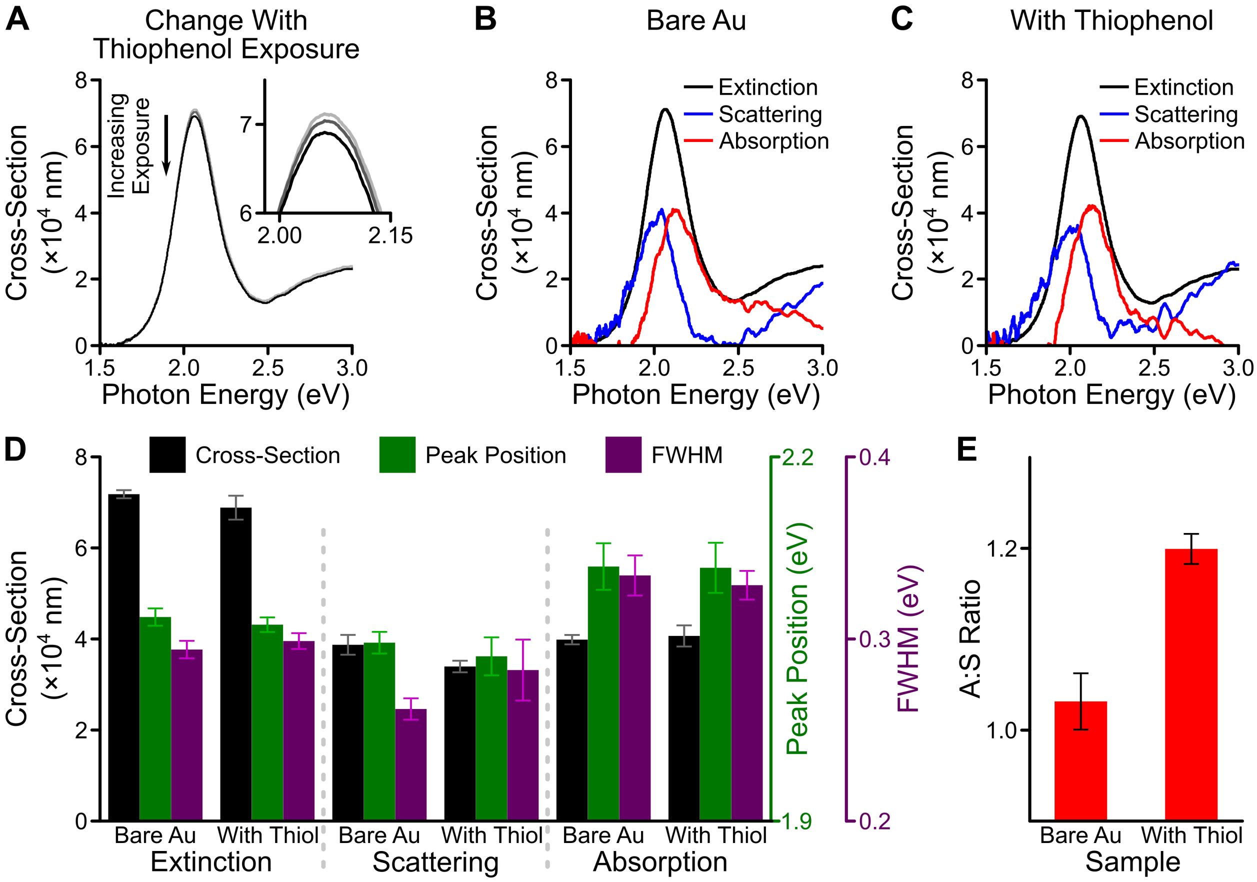

Figure 5. A) Series of extinction measurements showing spectral changes with increasing thiophenol exposure. The measured scattering and absorption contribution to extinction for B) bare Au nanodisks and C) after saturation adsorption of thiophenol. D) Quantification of changes to the optical cross-sections, peak position, and full-width-at-half-maximum (FWHM) for bare Au and thiophenol saturated samples. E) Absorption to scattering ratio before and after thiol adsorption. Reported values are the average of three separate measurements with the error bars representing the standard deviation.

Adsorption of thiophenol adds new electronic states at the surface of the Au nanodisks that are characterized by the hybridization of S and Au states. We propose that the new electronic states introduced by the chemical interface form new allowable interband electron transitions,[48] similar to *d*-band to *s,p*-band transitions in non-plasmonic metals.[49] In this way, the addition of a chemical interface makes the plasmonic material behave more like transition metals that do not have a full *d*-band. This is evidenced by an increase in the absorption to scattering ratio and a decrease in the overall extinction cross-section, which is more similar to non-coinage metals.[12,49] This mechanism is also consistent with the recent demonstration that Pt-decorated Ag nanocubes have a higher absorption-to-scattering ratio than pure Ag nanocubes.[50] Although in multimetallic nanostructures it can be difficult to determine the optical contributions of the different components, there is similarity in that the presence of new allowable interband transitions increases the absorption-to-scattering ratio in plasmonic materials. In the system presented here of thiophenol bound to Au, the influence by CID toward behavior of plasmonic materials to be more like other transition metals is not substantial enough to significantly impact the excellent light harvesting capability of the plasmonic nanoparticles. However, in more strongly coupled systems this effect may be so dramatic as to completely change the nature of the surface plasmon excitation.[11,24]

We hypothesize that the presence of new electronic states at the surface of plasmonic materials influences the electron distribution following surface plasmon dephasing; the distribution should be different for bare metals compared to metals dressed with chemical interfaces. The energy distribution of charge carriers upon initial surface plasmon dephasing should reflect the energy profile of allowable electronic transitions, specifically *s,p*-intraband transitions and metal-adsorbate interband transitions. This mechanism is consistent with ultrafast multi-electron photoemission studies showing that the hot electron distribution at chemical interfaces is sensitive to the energy of electron acceptor states.[25,26,51] Ultrafast transient absorption spectroscopy measurements also show that changing the surface chemistry of plasmonic nanoparticles can increase the hot electron lifetime.[52] Our results show that CID enhances the photon absorption-to-scattering ratio during surface plasmon dephasing, and suggests that photon absorption is localized at the chemical interface. Based on the direct involvement of adsorbate states in the CID plasmon dephasing pathway, it is hypothesized that CID should be a more efficient and energy specific charge transfer process for charge transfer at chemical interfaces compared to indirect carrier transfer, and therefore may play a more dominant role in photocatalysis and photovoltaics.

Conclusions

The photon scattering and absorption cross-sections of Au nanodisks were characterized before and after thiophenol adsorption to provide fundamental insight into the influence of a chemical interface on surface plasmon damping and dephasing. Thiophenol adsorption induced a decrease in the extinction coefficient, red-shift in the plasmon resonance energy, and spectral broadening. In particular, the measured broadening is quantifiably consistent with previous studies of the influence of alkanethiol adsorption on photon scattering by Au nanostructures. However, CID had almost no impact on the photon absorption plasmon dephasing pathway. The greater influence of CID on the photon scattering surface plasmon dephasing pathway relative to photon absorption leads to an increase in the absorption to scattering ratio. Our physical interpretation of the results is that the new electronic states associated with the adsorbed thiophenol present new surface plasmon dephasing pathways by interband electron transitions at the chemical interface. It is reasonable to expect the energy distribution of charge carriers to reflect the energy profile of allowable electronic transitions, and therefore should reflect the energy of the adsorbate states given the CID surface plasmon dephasing pathway of direct interband electron transfer. It is hypothesized that direct charge transfer to adsorbate states characteristic of the CID surface plasmon dephasing pathway should be a more efficient and bond selective mechanism of photocatalysis as compared to the indirect charge transfer pathway.

Conflicts of Interest

There are no conflicts to declare.

Acknowledgements

P.C. and N.J.H. acknowledge funding from the Air Force Office of Scientific Research MURI Grant FA9550-15-10022. PC acknowledges the Army Research Office Grants W911NF-17-1-0340 and W911NF-15-1-0321 for support in construction of the apparatus used to make measurements in these studies.

References

1 K. Watanabe, D. Menzel, N. Nilius and H.-J. Freund, *Chem. Rev.*, 2006, **106**, 4301–4320.

2 N. J. Halas, S. Lal, W. S. Chang, S. Link and P. Nordlander, *Chem. Rev.*, 2011, **111**, 3913–3961.

3 G. V. Hartland, *Chem. Rev.*, 2011, **111**, 3858–3887.

4 P. Christopher and M. Moskovits, *Annu. Rev. Phys. Chem.*, 2017, **68**, 379–398.

5 Y. Zhang, S. He, W. Guo, Y. Hu, J. Huang, J. R. Mulcahy and W. D. Wei, *Chem. Rev.*, 2018, **118**, 2927–2954.

6 U. Kreibig, M. Gartz and A. Hilger, *Berichte der Bunsengesellschaft für Phys. Chemie*, 1997, **101**, 1593–1604.

7 S. Link and M. A. El-Sayed, *J. Phys. Chem. B*, 1999, **103**, 4212–4217.

8 A. O. Govorov and H. Zhang, *J. Phys. Chem. C*, 2015, **119**, 6181–6194.

9 L. V. Besteiro and A. O. Govorov, *J. Phys. Chem. C*, 2016, **120**, 19329–19339.

10 S. Link and M. A. El-Sayed, *J. Phys. Chem. B*, 1999, **103**, 8410–8426.

11 G. V. Hartland, L. V. Besteiro, P. Johns and A. O. Govorov, *ACS Energy Lett.*, 2017, **2**, 1641–1653.

12 C. Langhammer, B. Kasemo and I. Zorić, *J. Chem. Phys.*, 2007, **126**, 194702.

13 B. N. J. Persson, *Surf. Sci.*, 1993, **281**, 153–162.

14 H. Petek, *J. Chem. Phys.*, 2012, **137**, 091704.

15 S. Linic, P. Christopher, H. Xin and A. Marimuthu, *Acc. Chem. Res.*, 2013, **46**, 1890–1899.

16 M. J. Kale, T. Avanesian and P. Christopher, *ACS Catal.*, 2014, **4**, 116–128.

17 M. J. Kale and P. Christopher, *Science*, 2015, **349**, 587–588.

18 D. Menzel, *J. Chem. Phys.*, 2012, **137**, 091702.

19 Q. Wei, S. Wu and Y. Sun, *Adv. Mater.*, 2018, 1802082.

20 T. Avanesian and P. Christopher, *J. Phys. Chem. C*, 2014, **118**, 28017–28031.

21 A. Listorti, B. O'Regan and J. R. Durrant, *Chem. Mater.*, 2011, **23**, 3381–3399.

22 C. Boerigter, R. Campana, M. Morabito and S. Linic, *Nat. Commun.*, 2016, **7**, 10545.

23 D. Menzel, K. H. Kim, D. Mulugeta and K. Watanabe, *J. Vac. Sci. Technol. A*, 2013, **31**, 050817.

24 K. Wu, J. Chen, J. R. McBride and T. Lian, *Science*, 2015, **349**, 632–635.

25 S. Tan, A. Argondizzo, J. Ren, L. Liu, J. Zhao and H. Petek, *Nat. Photonics*, 2017, **11**, 806–812.

26 S. Tan, Y. Dai, S. Zhang, L. Liu, J. Zhao and H. Petek, *Phys. Rev. Lett.*, 2018, **120**, 126801.

27 H. Hövel, S. Fritz, A. Hilger, U. Kreibig and M. Vollmer, *Phys. Rev. B*, 1993, **48**, 18178–18188.

28 A. Iline, M. Simon, F. Stietz and F. Träger, *Surf. Sci.*, 1999, **436**, 51–62.

29 C. Voisin, N. Del Fatti, D. Christofilos and F. Vallée, *J. Phys. Chem. B*, 2001, **105**, 2264–2280.

30 M. D. Malinsky, K. L. Kelly, G. C. Schatz and R. P. Van Duyne, *J. Am. Chem. Soc.*, 2001, **123**, 1471–1482.

31 C. Hendrich, J. Bosbach, F. Stietz, F. Hubenthal, T. Vartanyan and F. Träger, *Appl. Phys. B*, 2003, **76**, 869–875.

32 P. Zijlstra, P. M. R. Paulo, K. Yu, Q. H. Xu and M. Orrit, *Angew. Chemie - Int. Ed.*, 2012, **51**, 8352–8355.

33 J. Wei, N. Schaeffer and M.-P. Pileni, *J. Phys. Chem. B*, 2014, **118**, 14070–14075.

34 B. Foerster, A. Joplin, K. Kaefer, S. Celiksoy, S. Link and C. Sönnichsen, *ACS Nano*, 2017, **11**, 2886–2893.

35 T. Lünskens, A. Von Weber, M. Jakob, T. Lelaidier, A. Kartouzian and U. Heiz, *J. Phys. Chem. C*, 2017, **121**, 9331–9336.

36 S. W. Moon, P. V. Tsalu and J. W. Ha, *Phys. Chem. Chem. Phys.*, 2018, **20**, 22197–22202.

37 K. L. Kelly, E. Coronado, L. L. Zhao and G. C. Schatz, *J. Phys. Chem. B*, 2003, **107**, 668–677.

38 M. M. Miller and A. A. Lazarides, *J. Opt. A Pure Appl. Opt.*, 2006, **8**, S239–S249.

39 C. Langhammer, M. Schwind, B. Kasemo and I. Zoric, *Nano Lett.*, 2008, **8**, 1461–1471.

40 J. Olson, S. Dominguez-Medina, A. Hoggard, L.-Y. Wang, W.-S. Chang and S. Link, *Chem. Soc. Rev.*, 2015, **44**, 40–57.

41 C. Sönnichsen, T. Franzl, T. Wilk, G. von Plessen, J. Feldmann, O. Wilson and P. Mulvaney, *Phys. Rev. Lett.*, 2002, **88**, 77402.

42 V. Juvé, M. F. Cardinal, A. Lombardi, A. Crut, P. Maioli, J. Pérez-Juste, L. M. Liz-Marzán, N. Del Fatti and F. Vallée, *Nano Lett.*, 2013, **13**, 2234–2240.

43 H. Fredriksson, Y. Alaverdyan, A. Dmitriev, C. Langhammer, D. S. Sutherland, M. Zäch and B. Kasemo, *Adv. Mater.*, 2007, **19**, 4297–4302.

44 L.-J. Wan, M. Terashima, H. Noda and M. Osawa, *J. Phys. Chem. B*, 2000, **104**, 3563–3569.

45 J. Nara, S. Higai, Y. Morikawa and T. Ohno, *J. Chem. Phys.*, 2004, **120**, 6705–6711.

46 P. Maksymovych and J. T. Yates, *J. Am. Chem. Soc.*, 2008, **130**, 7518–7519.

47 A. Derkachova, K. Kolwas and I. Demchenko, *Plasmonics*, 2016, **11**, 941–951.

48 M. J. Kale, T. Avanesian, H. Xin, J. Yan and P. Christopher, *Nano Lett.*, 2014, **14**, 5405–5412.

49 I. Zorić, M. Zäch, B. Kasemo and C. Langhammer, *ACS Nano*, 2011, **5**, 2535–2546.

50 U. Aslam, S. Chavez and S. Linic, *Nat. Nanotechnol.*, 2017, **12**, 1000–1005.

51 J. Stähler, M. Mehlhorn, U. Bovensiepen, M. Meyer, D. O. Kusmierek, K. Morgenstern and M. Wolf, *Phys. Rev. Lett.*, 2007, **98**, 206105.

52 K. O. Aruda, M. Tagliazucchi, C. M. Sweeney, D. C. Hannah, G. C. Schatz and E. A. Weiss, *Proc. Natl. Acad. Sci.*, 2013, **110**, 1–6.

Table of contents entry

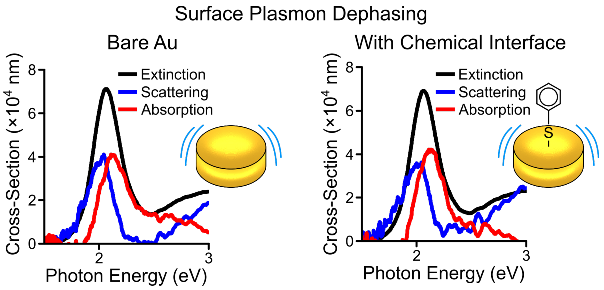

Characterized the change in photon absorption and scattering properties of plasmonic Au nanoparticles by chemical interface damping.